Journal of Materials Chemistry A

ROYAL SOCIETY OF CHEMISTRY

PAPER

View Article Online
View Journal | View Issue

Cite this: J. Mater. Chem. A, 2026, 14, 4396

Decoupling electrical conductivity and Seebeck coefficient *via* isoelectronic alloying in the 9-4-9-type $Ca_{9-y}Eu_yZn_{4.7}Sb_9$ ($0 \leq y \leq 5.0$) Zintl phase

Wenhua Xue,[ab] Chen Chen,[c] Pengfei Nan,[d] Youwen Long,[a] Binghui Ge,*[d] Qian Zhang*[b] and Yumei Wang*[ae]

Thermoelectric materials face a fundamental challenge due to the strong coupling between electrical conductivity and Seebeck coefficient. Here, we demonstrate that Eu alloying in the 9-4-9-type Zintl phase $Ca_{9-y}Eu_yZn_{4.7}Sb_9$ ($0 \leq y \leq 5.0$) gives rise to an "intergrowth" structure, which effectively decouples these properties. Advanced characterization techniques, including electron energy loss spectroscopy (EELS) and X-ray absorption spectroscopy (XAS), reveal that the valence state of Eu in this "intergrowth" structure is a mixture of +2 and +3. The "intergrowth" structure with Eu^{3+} reduces carrier concentration, thereby enhancing the Seebeck coefficient. Concurrently, C_s-corrected transmission electron microscopy (TEM) quantitatively demonstrates that the intensity of interstitial Zn atoms gradually increases with Eu alloying, improving carrier mobility and boosting electrical conductivity. Consequently, a simultaneous enhancement of both the Seebeck coefficient (from 113 μV K^{-1} to 121 μV K^{-1}) and electrical conductivity (from 2.5×10^4 S m^{-1} to 3.26×10^4 S m^{-1}) is achieved in the 9-4-9-type $Ca_{9-y}Eu_yZn_{4.7}Sb_9$ Zintl phase and the underlying mechanism behind the effective decoupling is uncovered. Our findings provide a new pathway for optimizing thermoelectric performance, offering valuable insights for the design of high-performance thermoelectric materials.

Received 31st May 2025
Accepted 6th November 2025

DOI: 10.1039/d5ta04387e

rsc.li/materials-a

Introduction

Thermoelectric (TE) materials, which enable the direct conversion of heat into electricity, have received significant attention due to their potential in energy harvesting and waste heat recovery.[1–3] The performance of TE materials is governed by the dimensionless figure of merit zT, defined as $zT = S^2\sigma T/(\kappa_e + \kappa_L)$, where S is the Seebeck coefficient, σ is the electrical conductivity, T is the absolute temperature, κ_e is the electronic thermal conductivity, and κ_L is the lattice thermal conductivity.[4–7] However, improving zT remains challenging due to the strong coupling between these transport parameters.[8–11] The electrical transport properties of TE materials, including electrical conductivity, Seebeck coefficient, and electronic thermal conductivity, are strongly coupled through carrier concentration.[12,13] Therefore, achieving an optimal carrier concentration is crucial for balancing these parameters and enhancing thermoelectric performance. One effective strategy to tune carrier concentration is through the substitution of heterovalent or isovalent elements.[12–18] For example, Br doping (6–12 atm%) on the Se site in SnSe significantly increases the carrier concentration from 1.6×10^{17} cm^{-3} (p-type) to 1.3×10^{19} cm^{-3} (n-type) in Br-doped $SnSe_{0.88}Br_{0.12}$, leading to a substantial improvement in electrical conductivity.[19] Similarly, substitution of Bi with cerium (Ce) in the Bi_2Se_3 TE material effectively controls carrier concentration, optimizing both electrical conductivity and Seebeck coefficient.[20]

Zintl phases, which can exhibit "phonon glass, electron crystal" behavior and complex polyanionic structures, have emerged as promising candidates for TE materials due to their intrinsic low lattice thermal conductivity and good electrical conductivity.[18,21–24] Among them, the 9-4-9-type Zintl phase $Ca_9Zn_{4+x}Sb_9$ has shown potential for high thermoelectric performance owing to its complex crystal structure and tunable interstitial atoms.[25–27] Previous studies have demonstrated that substituting Eu for Ca in this system can not only reduce the lattice thermal conductivity but also enhance carrier mobility, attributed to a decrease in effective mass and an increase in interstitial Zn atoms.[28,29] Furthermore, Eu alloying can induce structural transformations, such as the transition from the 9-4-9 phase (space group *Pbam*) to the 2-1-2 phase (space group $P6_3/mmc$), which exhibits extremely low lattice thermal conductivity and a higher zT value.[30] However, the physical mechanisms by

[a]Institute of Physics, Chinese Academy of Sciences, Beijing 100190, China. E-mail: wangym@iphy.ac.cn
[b]School of Materials Science and Engineering, Harbin Institute of Technology, Shenzhen 518055, China
[c]School of Physical Sciences, Great Bay University, Dongguan, 523000, China
[d]Institutes of Physical Science and Information Technology, Anhui University, Hefei 230601, China
[e]Beijing Branch of Songshan Lake Materials Laboratory, Beijing 100190, China

which Eu alloying affects carrier concentration, mobility, and overall transport properties remain poorly understood.

Here, we investigate the effect of Eu alloying on the thermoelectric properties of the $Ca_{9-y}Eu_yZn_{4.7}Sb_9$ system, focusing on the decoupling of the electrical conductivity and Seebeck coefficient. By systematically varying the Eu content in $Ca_{9-y}Eu_yZn_{4.7}Sb_9$ ($0 \le y \le 5.0$), we uncover an "intergrowth" structure that significantly enhances the thermoelectric performance. Using advanced characterization techniques such as C_s-corrected transmission electron microscopy (TEM), electron energy loss spectroscopy (EELS) and X-ray absorption spectroscopy (XAS), we demonstrate that the valence state of Eu in the "intergrowth" structure is a mixture of +2 and +3, in which Eu^{3+} reduces carrier concentration, further enhancing the Seebeck coefficient. The introduction of Eu leads to an increase in interstitial Zn atoms and a reduction in effective mass, both of which significantly enhance the carrier mobility and electrical conductivity. This dual effect leads to a simultaneous enhancement of the Seebeck coefficient and electrical conductivity. Our findings not only elucidate the decoupling mechanisms of the electrical conductivity and Seebeck coefficient in 9-4-9-type Zintl phases but also highlight the potential of isoelectronic alloying as a powerful strategy for designing high-performance thermoelectric materials.

Results and discussion

To investigate the Eu alloying on the structures and thermoelectric properties, a series of compounds $Ca_{9-y}Eu_yZn_{4.7}Sb_9$ ($0 \le y < 9.0$) and $Ca_{9-y}Eu_yZn_{4.41}Sb_9$ ($y = 9.0$) were synthesized and characterized by X-ray diffraction (XRD) (Fig. 1). The XRD results reveal that the 9-4-9 structure, like that of $Ca_9Zn_{4.5}Sb_9$, is maintained for Eu contents up to $y = 5.0$. However, when the Eu content exceeds 5.05, the material begins to transition toward the 2-1-2 phase ($P6_3/mmc$). In $Ca_{9-y}Eu_yZn_{4.7}Sb_9$ ($y = 5.05$), diffraction peaks corresponding to both the 9-4-9 orthorhombic structure and the 2-1-2 hexagonal structure are observed, indicating a two-phase coexistence. As the Eu content further increases, the 9-4-9 phase gradually diminishes, while the 2-1-2 phase becomes dominant (see Fig. S1). Complete transformation into the 2-1-2 phase occurs when Eu fully replaces Ca ($y = 9.0$). The XRD data indicate that $Ca_{9-y}Eu_yZn_{4.7}Sb_9$ compounds with $y \le 5.0$ retain the 9-4-9-type Zintl phase structure, while the 2-1-2 phase becomes the primary phase for $y > 5.05$. Given the focus of this study on the 9-4-9-type structure, subsequent analyses and discussions are centered on compounds with $y \le 5.0$.

Electrical transport properties

The temperature-dependent electrical conductivities and Seebeck coefficients were measured for compounds $Ca_{9-y}Eu_yZn_{4.7}Sb_9$ ($y = 0$, 1.125, 3.375, 5.0, 5.05) and $Ca_{9-y}Eu_yZn_{4.41}Sb_9$ ($y = 9.0$), and the results are presented (Fig. 2a and b). Compared to the undoped $Ca_9Zn_{4.7}Sb_9$, the electrical conductivity and Seebeck coefficient of $Ca_{9-y}Eu_yZn_{4.7}Sb_9$ ($y = 1.125$, 3.375, 5.0) generally increase with increase in Eu content, indicating

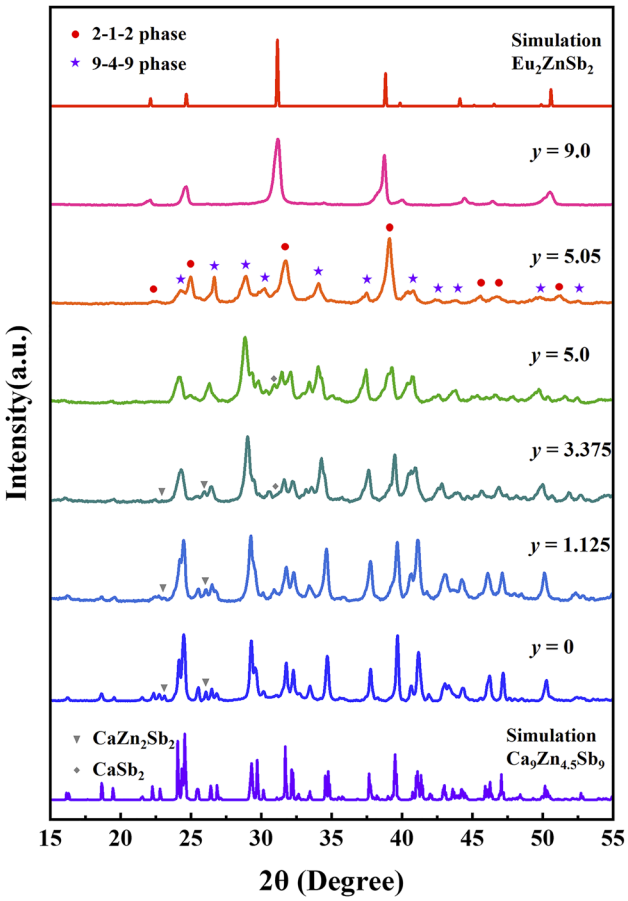

Fig. 1 XRD patterns for $Ca_{9-y}Eu_yZn_{4.7}Sb_9$ ($y = 0$, 1.125, 3.375, 5.0, 5.05) and $Ca_{9-y}Eu_yZn_{4.41}Sb_9$ ($y = 9.0$) samples with pentagrams and dots indicating the 9-4-9 phase and the 2-1-2 phase, respectively.

a simultaneous enhancement of these properties in the 9-4-9 phase. However, when the Eu content reaches $y = 5.05$, the crystal structure begins to transform from the 9-4-9 phase into the 2-1-2 phase. At this point, while the Seebeck coefficient continues to increase, the electrical conductivity decreases. This trend becomes more evident as the Eu alloying content goes up to $y = 9.0$, where the material fully transforms into the 2-1-2 phase.

In the 9-4-9-type $Ca_{9-y}Eu_yZn_{4.7}Sb_9$ compounds ($y \le 5.0$), the simultaneous increase in the Seebeck coefficient and electrical conductivity suggests an effective decoupling of these two properties, leading to a significant improvement in the power factor compared to undoped $Ca_9Zn_{4.7}Sb_9$, as shown in Fig. 2c. This decoupling is attributed to the interplay between carrier concentration (n_H) and mobility (μ_H), as described by the following equations for degenerated semiconductors:

$$S = \frac{8\pi^2 k_B^2}{3eh^2} m^* T \left(\frac{\pi}{3n_H}\right)^{2/3}$$

and

$$\sigma = n_H \mu_H e$$

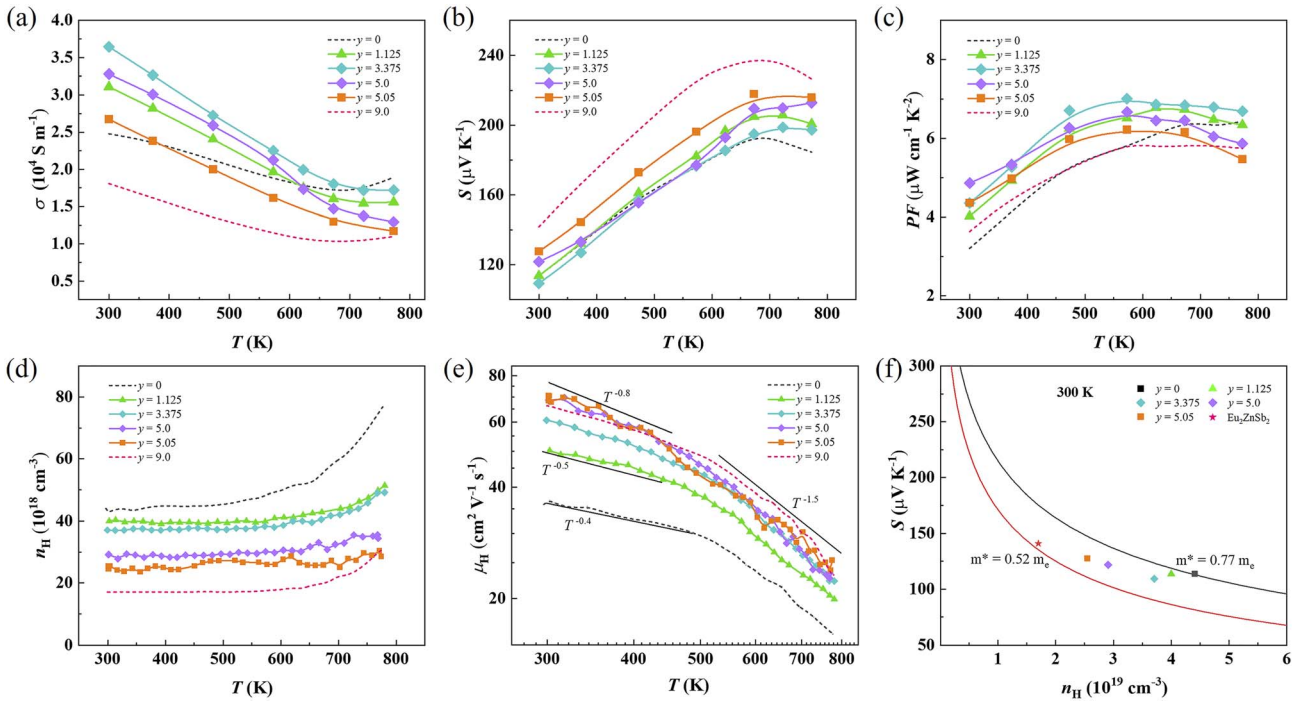

Fig. 2 Electrical transport performances for $Ca_{9-y}Eu_yZn_{4.7}Sb_9$ (y = 0, 1.125, 3.375, 5.0, 5.05) and $Ca_{9-y}Eu_yZn_{4.41}Sb_9$ (y = 9.0). Temperature-dependent (a) electrical conductivity, (b) Seebeck coefficient, (c) power factor, (d) Hall carrier concentration, (e) Hall mobility and (f) room-temperature Pisarenko relationships.

where k_B, h, m^* and e are the Boltzmann constant, Planck constant, effective mass, and electron charge, respectively. These equations highlight the strong coupling between the Seebeck coefficient and electrical conductivity through the carrier concentration. With increasing Eu content, we observed three key trends: (1) a decrease in carrier concentration (Fig. 2d), (2) an increase in mobility (Fig. 2e) and (3) a reduction in effective mass from approximately 0.77 m_0 to 0.52 m_0 (Fig. 2f), calculated based on the single parabolic band (SPB) model.[28] Typically, a decrease in effective mass enhances Hall mobility,

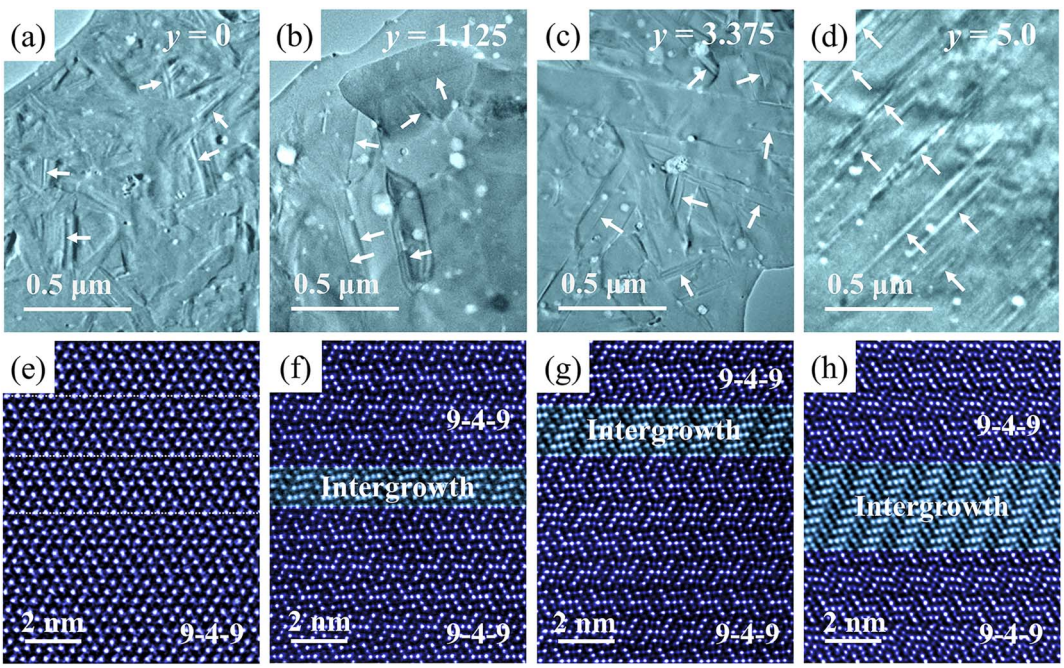

Fig. 3 (a–d) Low-magnification TEM for 9-4-9-type $Ca_{9-y}Eu_yZn_{4.7}Sb_9$ (y = 0, 1.125, 3.375, 5.0) and (e–h) [001] HAADF-STEM images corresponding to a–d.

thereby improving electrical conductivity but reducing the Seebeck coefficient. Conversely, a reduction in carrier concentration tends to lower the electrical conductivity while increasing the Seebeck coefficient. In the 9-4-9-type $Ca_{9-y}Eu_yZn_{4.7}Sb_9$ compounds, the increase in Seebeck coefficient is primarily driven by the decrease in carrier concentration, while the increase in electrical conductivity is mainly due to the enhanced mobility.

Formation and characterization of the "intergrowth" structure

It is well known that the structure of a material determines its properties. To elucidate the underlying mechanism of simultaneous increase in the Seebeck coefficient and electrical conductivity (Fig. 2), we employed TEM to characterize the microstructural features of 9-4-9-type $Ca_{9-y}Eu_yZn_{4.7}Sb_9$ compounds. Fig. 3a–d show typical low-magnification TEM images of $Ca_{9-y}Eu_yZn_{4.7}Sb_9$ (y = 0, 1.125, 3.375, 5.0) compounds, revealing lath-like grains with distinct string-like contrasts (marked by arrows). Further investigation using high-angle annular dark field scanning transmission electron microscopy (HAADF-STEM) provides structural information at the atomic level (see Fig. 3e–h). In the undoped sample ($y = 0$), the string-like contrasts are identified as 180° domains, as marked in Fig. 3e, while for $y = 1.125, 3.375, 5.0$, these contrasts are identified as the "intergrowth" structures, as observed in the [001] HAADF-STEM images (Fig. 3f–h). These "intergrowth" structures are fully coherent with the 9-4-9 phase and gradually increase with increasing Eu content.

The "intergrowth" structure, which is composed of Ca, Eu, Zn, and Sb elements (Fig. S2), was not detected *via* XRD (Fig. 1) due to its relatively low volume fraction in $Ca_{9-y}Eu_yZn_{4.7}Sb_9$ (y = 1.125, 3.375, 5.0, 5.05). Semi-quantitative EDS analysis of this region indicates an average atomic composition ratio of approximately (Ca + Eu) : Zn : Sb ≈ 3 : 1 : 3. This composition is different from the parent $Ca_9Zn_{4.5}Sb_9$ and Eu_2ZnSb_2 phases, providing strong support for the formation of an intergrowth structure.

Valence state of Eu in the "intergrowth" structure

XAS was performed to explore the valence state of Eu in $Ca_{9-y}Eu_yZn_{4+\delta}Sb_9$ compounds. Fig. 4 shows the Eu L_3-edge XAS spectra for $Ca_{9-y}Eu_yZn_{4.7}Sb_9$ (y = 1.125, 3.375, 5.0) and $Ca_{9-y}Eu_yZn_{4.41}Sb_9$ (y = 9.0), with Eu_2O_3 as a reference for the Eu^{3+} peak at 6984.4 eV. For y = 9.0, the spectrum exhibits a single peak at 6976.2 eV, consistent with the feature of Eu^{2+} as reported in compounds $Eu(O_3SCF_3)_2$ and Eu-doped $Sr_2MgSi_2O_7$.[31–33] However, for y = 1.125, 3.375, 5.0, a shoulder at 6984.4 eV appears alongside the Eu^{2+} peak, consistent with the main peak energy of Eu_2O_3, indicating the presence of Eu^{3+}. This Eu^{3+} character becomes more pronounced at y = 5.0, while the amplitude of the Eu^{2+} peak decreases with increasing Eu content.

The observation of Eu^{3+} in a Zintl phase is unusual, as its electronic configuration typically adheres to the Zintl–Klemm concept.[34] However, this is not without precedent. For instance, the co-existence of Yb^{2+} and Yb^{3+} has been unambiguously confirmed *via* XAS in the related $Yb_{14}ZnSb_{11}$ Zintl phase.[35] We note that the spectral features (Fig. 2 in ref. 35) exhibit remarkable similarity to our results (Fig. 4), providing strong circumstantial evidence for the presence of mixed Eu^{2+}/Eu^{3+} valence in our samples.

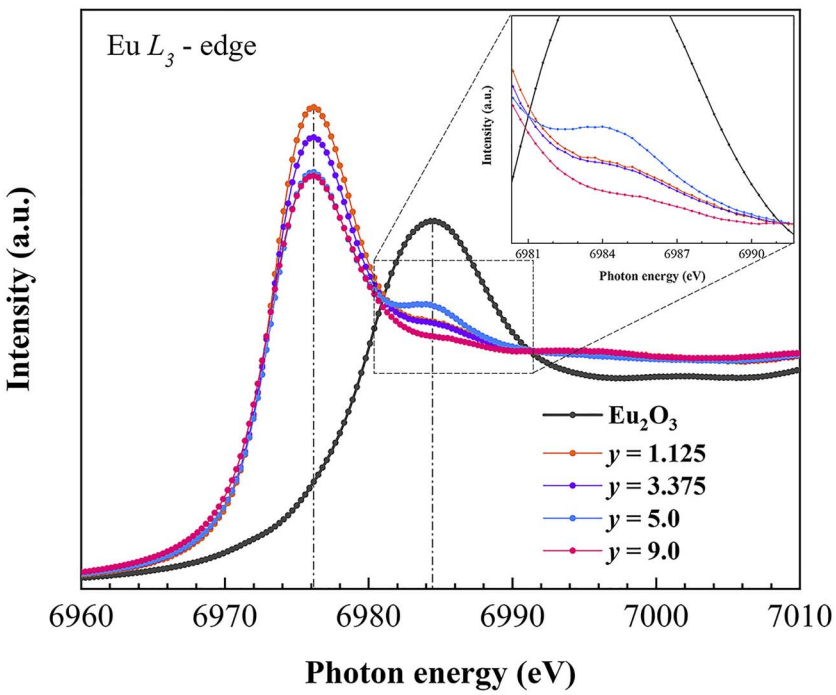

Fig. 4 Eu L_3-edge XAS spectra for Eu_2O_3, $Ca_{9-y}Eu_yZn_{4.7}Sb_9$ (y = 1.125, 3.375, 5.0) and $Ca_{9-y}Eu_yZn_{4.41}Sb_9$ (y = 9.0). An enlarged view of the rectangular area in the inset.

Based on this, we consider the presence of Eu^{3+} in the material to be reasonable. To compensate for the extra positive charge introduced by Eu^{3+} (*i.e.*, to provide the necessary electrons), the system appears to respond through several interconnected mechanisms: (1) the reduction in hole carrier concentration, as evidenced by Hall effect measurements (Fig. 2d), where electrons from Eu^{3+} compensation neutralize holes in the p-type matrix; (2) the formation of defects or new phases that can modulate local charge, such as the observed "intergrowth" structure which accommodates Eu^{3+} ions while maintaining structural stability. Therefore, the hypothesis of the intergrowth phase acting as an "Eu^{3+} sink" forms a self-consistent interpretive model together with the XAS data and electronic transport properties.

To experimentally verify this hypothesis and pinpoint the origin of Eu^{3+}, we further investigated the electronic structure of $Ca_{9-y}Eu_yZn_{4.7}Sb_9$ ($y = 5.05$) using TEM and EELS. Fig. 5a shows a typical low-magnification TEM image of this composition, where grains of different morphologies labeled A, B and C are clearly visible. The C_s-corrected HAADF-STEM images (inset in Fig. 5a) reveal that these grains correspond to the 9-4-9 phase (A), the "intergrowth" structure (B) and the 2-1-2 phase (C),[30] respectively. This indicates that at $y = 5.05$, the 9-4-9 phase, 2-1-2 phase and "intergrowth" structures coexist. The "intergrowth" structure exists as nanoscale domains embedded in the bulk matrix of the 9-4-9 phase $Ca_{9-y}Eu_yZn_{4.7}Sb_9$ ($y \leq 5.0$), and its volume fraction increases with higher Eu content. When the Eu content increases to $y = 5.05$, the "intergrowth" structure in the material further expands and forms an independent grain, as shown in Fig. 5a. This composition was selected for EELS investigation because it allows coexistence of the "intergrowth" structure with both the 9-4-9 phase and 2-1-2 phase. Fig. 5b is the Eu $N_{4,5}$-edge EELS spectra obtained from grains A, B and C in Fig. 5a, along with a reference spectrum of Eu_2O_3 (Eu^{3+}). The Eu^{3+} spectrum of Eu_2O_3 is characterized by sharp peaks at 142.3 eV (I) and 150 eV (II). In contrast, the spectra of the 9-4-9 phase and 2-1-2 phase exhibit two distinct peaks at ~140 eV (I) and ~134 eV (III). Compared to Eu_2O_3, peak I in both phases shows a chemical shift of ~2 eV toward lower energy, suggesting that the valence state of Eu in these two phases is less than +3. Based on the XAS results (Fig. 4), the valence state of Eu in the 2-1-2 phase is bivalent (Eu^{2+}), implying that the valence state of Eu in the 9-4-9 phase is also bivalent. However, the EELS spectra of the "intergrowth" structure exhibits all three characteristic peaks (I, II and III), with peaks I and II matching those of Eu_2O_3. This indicates a mixed valence state of Eu^{2+} and Eu^{3+} in the "intergrowth" structure.

Carrier concentration reduction *via* Eu^{3+}

The formation of the "intergrowth" structure is closely related to the mixed valence state of Eu. Based on the charge compensation modulation, when the oxidation state of certain elements in the material changes, the system maintains overall charge neutrality by adjusting the concentration of other charge carriers (electrons or holes) or introducing defects (such as vacancies). This phenomenon is widely observed in doped semiconductors[36,37] and oxide materials.[38,39] In 9-4-9-type $Ca_{9-y}Eu_yZn_{4.7}Sb_9$ compounds, the primary carriers are holes. The presence of Eu^{3+} in the "intergrowth" structure acts as an n-type dopant, generating electrons that neutralize holes through charge compensation. This process effectively reduces the hole concentration, thereby enhancing the Seebeck coefficient. The Eu^{3+} peak intensity correlates with the density of "intergrowth" structures, reaching its maximum at $y = 5.0$ (Fig. 3d), where the highest Seebeck coefficient is observed (Fig. 2b).

Role of interstitial Zn atoms in modulating carrier concentration and enhancing mobility

In 9-4-9-type Zintl compounds $Ca_{9-y}Eu_yZn_{4.7}Sb_9$, the anionic framework provides a pathway for carrier transport. This is facilitated by one-dimensional $[Zn_4Sb_9]^{19-}$ ribbon-like chains that connect with partially occupied interstitial Zn sites to form pseudo two-dimensional layers,[18,25–27,40] as shown in Fig. 6a. The

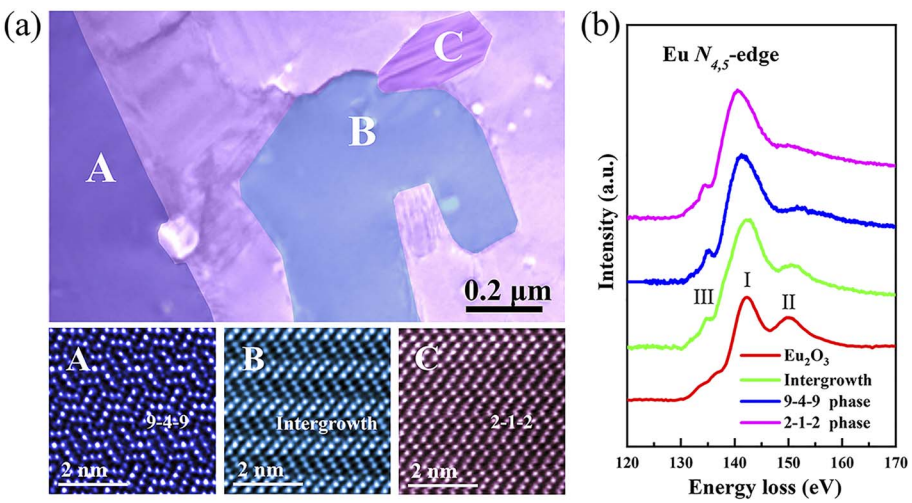

Fig. 5 (a) Low-magnification TEM for $Ca_{9-y}Eu_yZn_{4.7}Sb_9$ ($y = 5.05$) with HAADF-STEM images of A, B and C in the inset. (b) Eu $N_{4,5}$-edge EELS spectra obtained from A, B and C image regions in (a), respectively, and the standard spectrum of Eu_2O_3.

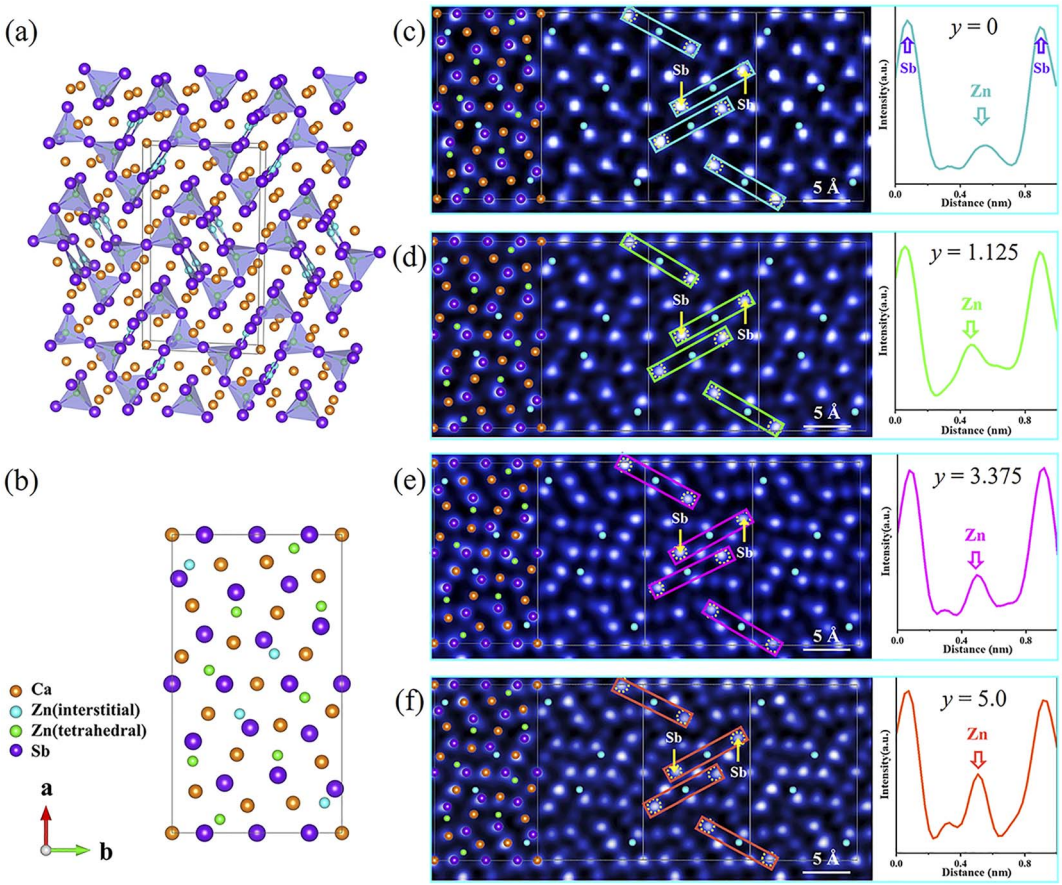

Fig. 6 (a) Structural model with the unit cell outlined and (b) [001] structural projection of $Ca_9Zn_{4.5}Sb_9$; Ca, Zn, and Sb are shown as orange, green, and purple spheres, respectively. [001] HAADF-STEM images for $Ca_{9-y}Eu_yZn_{4.7}Sb_9$ (c) $y = 0$, (d) $y = 1.125$, (e) $y = 3.375$ and (f) $y = 5.0$. Solid circles represent the interstitial Zn sites, while dashed circles indicate the Sb sites. The intensity profiles are obtained by scanning along the lines passing through the center of the interstitial Zn atom and two Sb atoms within the boxes.

more interstitial Zn atoms that join the Zn_4Sb_9 ribbons, the more freely carriers pass through, thereby optimizing the mobility and electrical conductivity.

To quantitatively investigate the evolution of interstitial Zn, we performed the atomic-resolution HAADF-STEM imaging technique. Along the [001] projection (Fig. 6b) of $Ca_{9-y}Eu_yZn_{4.7}Sb_9$ compounds, Ca, Zn, and Sb are separately distinguishable, making it suitable for studying interstitial Zn atoms *via* TEM. Fig. 6c–f show [001] HAADF-STEM images of $Ca_{9-y}Eu_yZn_{4.7}Sb_9$ ($y = 0$, 1.125, 3.375, and 5.0), with interstitial Zn atoms marked by solid circles. As the Eu content increases, the intensity of interstitial Zn atoms gradually increases, as quantitatively demonstrated by the intensity profile on the right side of the images. These profiles were obtained by scanning along a line passing through the center of the interstitial Zn atom and two Sb atoms, with the intensity of Sb normalized to unity. The intensity of atoms is derived from the average intensity measured at equivalent interstitial Zn positions within the unit cell of $Ca_{9-y}Eu_yZn_{4.7}Sb_9$. The intensity peaks of interstitial Zn atoms increase as Eu content rises. This trend is supported by XRD data (Fig. 1), which show a leftward shift in the peaks of $Ca_{9-y}Eu_yZn_{4.7}Sb_9$ ($y = 1.125$, 3.375, and 5.0), indicating lattice expansion with increasing Eu content. This expansion provides more space for interstitial Zn atoms, further enhancing their concentration.

The incorporation of interstitial Zn, along with the charge compensation effect associated with the presence of Eu^{3+}, contributes to a reduction in hole carrier concentration, thereby enhancing the Seebeck coefficient. Concurrently, the enhanced connectivity between Zn_4Sb_9 chains *via* interstitial Zn transforms the carrier transport pathway from a one-dimensional chain-like regime to a more continuous two-dimensional framework, leading to a significant improvement in carrier mobility. This dual effect—carrier concentration reduction and mobility enhancement—enables the concurrent increase in both the Seebeck coefficient and electrical conductivity, as observed in our measurements. Our work provides the experimental evidence that Eu alloying promotes the increase of interstitial Zn atoms, which in turn plays a decisive role in decoupling the Seebeck coefficient and the electrical conductivity in 9-4-9 Zintl phases.

Conclusions

We have demonstrated that Eu alloying in 9-4-9-type $Ca_{9-y}Eu_yZn_{4.7}Sb_9$ ($0 \leq y \leq 5.0$) induces an "intergrowth" structure, which

plays a critical role in decoupling electrical conductivity and the Seebeck coefficient. Through systematic investigation of Eu-alloyed $Ca_{9-y}Eu_yZn_{4.7}Sb_9$ Zintl phases, we reveal the "intergrowth" structure that effectively decouples electrical conductivity and the Seebeck coefficient. Comprehensive characterization using C_s-corrected TEM, EELS, and XAS demonstrates that the presence of Eu^{3+} in this unique structure simultaneously reduces carrier concentration while enhancing the Seebeck coefficient. Furthermore, Eu alloying increases the concentration of interstitial Zn atoms in the 9-4-9-type $Ca_{9-y}Eu_yZn_{4.7}Sb_9$, which also contributes to a reduction in hole carrier concentration, thereby enhancing the Seebeck coefficient. Concurrently, these interstitial Zn atoms serve as a bridge connecting the Zn_4Sb_9 anion chains, facilitating carrier mobility, and consequently enhancing the electrical conductivity.

While mechanisms such as band engineering or energy filtering could contribute to the property enhancements, the simultaneous trends of (a) increasing Eu^{3+} content, (b) decreasing carrier concentration (n_H), and (c) a growing volume fraction of the intergrowth structure with increasing Eu doping strongly indicate that charge compensation mediated by the mixed $Eu^{2+/3+}$ valence is the dominant mechanism. Our findings establish a clear structure–property relationship, elucidating the decoupling mechanism responsible for the superior thermoelectric performance in these Zintl phases. This work not only validates isoelectronic alloying as an effective design strategy for high-performance thermoelectric materials, but also provides a fundamental framework for optimizing charge transport properties in complex Zintl compounds.

Experimental

Ca (99.9%, shots), Eu (99.9%, chunks), Zn (99.999%, powder), and Sb (99.999%, shots) were weighed according to the stoichiometry of $Ca_{9-y}Eu_yZn_{4+\delta}Sb_9$ ($y = 0$, 1.125, 3.375, 5.0, 5.05, 5.3, 5.5, 6.0, 6.75 and 9.0). To compensate for Zn loss during hot pressing (as the melting temperature of Zn exceeds the processing temperature),[25] a Zn-rich nominal composition ($\delta = 0.7$) was used for synthesizing $Ca_{9-y}Eu_yZn_{4+\delta}Sb_9$ ($y \leq 6.75$). For the $y = 9.0$ composition, which forms the 2-1-2 phase Eu_2ZnSb_2, the nominal Zn content was moderated to $\delta = 0.41$ to prevent the formation of the $EuZn_2Sb_2$ secondary phase.[30] The raw materials (total weight ~4 g) were loaded into a stainless-steel jar with stainless steel balls in an argon-filled glovebox and then ball-milled (SPEX 8000 M) continuously for 10 h. The obtained powder was loaded into a graphite die with an inner diameter of 12.7 mm with direct current (DC) hot pressing for 2 min under an axial pressure of 50 MPa at 973 K.

The crystal structures were determined by X-ray diffraction (XRD, Rigaku D/max 2500 PC, with Cu Kα radiation $\lambda = 1.5418$ Å). S and σ were simultaneously measured on a commercial apparatus (CTA-3, CRYALL). The temperature-dependent Hall coefficient (R_H) was measured using the van der Pauw technique on a commercial variable-temperature Hall effect measurement system (CRYALL, China) under a reversible magnetic field of 1.5 T. The Hall carrier concentration n_H and Hall mobility μ_H were calculated using $n_H = 1/(eR_H)$ and $\mu_H = \sigma R_H$, respectively.

The specimens for TEM observation were prepared by mechanical polishing, dimpling, and then by Ar^+ ion milling at 2.0 kV in a liquid nitrogen environment. TEM and HAADF-STEM investigations were carried out using a JEM-ARM 200F electron microscope equipped with a cold FEG source and double-C_s correctors, respectively. The attainable spatial resolution of the microscope is 80 pm. All the HAADF-STEM images presented in this work have been Fourier-filtered to reduce the random noise. EELS and EDS were carried out using an FEI Titan Themis Z microscope equipped with a probe and image correctors operated at 300 kV. The XAS was adopted for determining the valence states of Eu at beamline BL16A of the National Synchrotron Radiation Research Center (NSRRC) in Taiwan, using the total electron yield (TEY) mode.

Author contributions

W. H. X. and Y. M. W. designed the research and wrote the paper. C. C. synthesized the samples and carried out the XRD characterization and thermoelectric property measurements. P. F. N. and B. H. G. carried out the EELS and EDS characterization. Y. W. L. carried out the XAS characterization. Q. Z. and Y. M. W. were involved in funding acquisition.

Conflicts of interest

The authors declare no conflict of interest.

Data availability

Additional data related to this paper may be requested from the authors.

All data needed to evaluate the conclusions in the paper are present in the paper and/or the supplementary information (SI). Supplementary information is available. See DOI: https://doi.org/10.1039/d5ta04387e.

Acknowledgements

This work was supported by the National Natural Science Foundation of China (No. 12374021, 12074409, and 52172194) and the Beijing Natural Science Foundation (No. 1252031).

References

1 Y. Wang, L. Yang, X. L. Shi, X. Shi, L. Chen, M. S. Dargusch, J. Zou and Z.-G. Chen, *Adv. Mater.*, 2019, **31**, 1807916.
2 Y. Xing, R. Liu, J. Liao, C. Wang, Q. Zhang, Q. Song, X. Xia, T. Zhu, S. Bai and L. Chen, *Joule*, 2020, **4**, 2475–2483.
3 X. L. Shi, J. Zou and Z.-G. Chen, *Chem. Rev.*, 2020, **120**, 7399–7515.
4 J. He and T. Tritt, *Science*, 2017, **357**, eaak9997.
5 Y. Pei, H. Wang and G. B. Snyder, *Adv. Mater.*, 2012, **24**, 6125–6135.

6 W. Liu, J. Hu, S. Zhang, M. Deng, C. G. Han and Y. Liu, *Mater. Today Phys.*, 2017, **1**, 50–60.
7 G. Chen, M. Dresselhaus, G. Dresselhaus, J. P. Fleurial and T. Caillat, *Int. Mater. Rev.*, 2003, **48**, 45–66.
8 G. J. Snyder and E. Toberer, *Nat. Mater.*, 2008, **7**, 105–114.
9 D. Z. Wang, W. D. Liu, Y. Mao, S. Li, L. C. Yin, H. Wu, M. Li, Y. Wang, X. L. Shi, X. Yang, Q. Liu and Z. Chen, *J. Am. Chem. Soc.*, 2024, **146**, 1681–1689.
10 L. Su, D. Wang, S. Wang, B. Qin, Y. Wang, Y. Qin, Y. Jin, C. Chang and L.-D. Zhao, *Science*, 2022, **375**, 1385–1389.
11 P. L. Wang, T. Kolodiazhnyi, J. Yao and Y. Mozharivskyj, *J. Am. Chem. Soc.*, 2012, **134**, 1426–1429.
12 X. Shi, T. Zhao, X. Zhang, C. Sun, Z. Chen, S. Lin, W. Li, H. Gu and Y. Pei, *Adv. Mater.*, 2019, **31**, 1903387.
13 X. Wang, J. Li, C. Wang, B. Zhou, L. Zheng, B. Gao, Y. Chen and Y. Pei, *Chem. Mater.*, 2018, **30**, 5339–5345.
14 Y. Liu, L.-D. Zhao, Y. Zhu, Y. Liu, F. Li, M. Yu, D. B. Liu, W. Xu, Y. H. Lin and C. Nan, *Adv. Energy Mater.*, 2016, **6**, 1502423.
15 X. Wang, W. Li, C. Wang, J. Li, X. Zhang, B. Zhou, Y. Chen and Y. Pei, *J. Mater. Chem. A*, 2017, **5**, 24185–24192.
16 Y. Pei, A. LaLonde, S. Iwanaga and G. J. Snyder, *Energy Environ. Sci.*, 2011, **4**, 2085–2089.
17 X. Li, J. J. Yu, Y. T. Liu, Z. Wu, J. Guo, T. J. Zhu, X. B. Zhao, X. T. Tao and S. Q. Xia, *Inorg. Chem. Front.*, 2017, **4**, 1113–1119.
18 M. Zhu, Z. Wu, Q. Liu, T.-J. Zhu, X. Zhao, B. Huang, X. Tao and S.-Q. Xia, *J. Mater. Chem. A*, 2018, **6**, 11773–11782.
19 S. Li, Y. Wang, C. Chen, X. Li, W. Xue, X. Wang, Z. Zhang, F. Cao, J. Sui, X. Liu and Q. Zhang, *Adv. Sci.*, 2018, **5**(9), 1800598.
20 J.-D. Musah, Y. Xiao, A. M. Ilyas, T. G. Novak, S. Jeon, C. Arava, S. V. Novikov, D. S. Nikulin, W. Xu, L. Liu, M. Asaduzzaman, K.-H. Lam, X. F. Chen, C.-M. L. Wu and V. A. L. Roy, *ACS Appl. Mater. Int.*, 2019, **11**, 44026–44035.
21 E. Toberer, A. May and G. Snyder, *Chem. Mater.*, 2010, **22**, 624–634.
22 J. Shuai, H. S. Kim, Z. Liu, R. He, J. Sui and Z. Ren, *Appl. Phys. Lett.*, 2016, **108**, 183901.
23 G. A. Slack and D. Rowe, *CRC thermoelectrics handbook*, CRC press, Boca Raton FL, 1995.
24 S. Fang, J. Li, K. Zou, H. Shuai, L. Xu, W. Deng, G. Zou, H. Hou and X. Ji, *Chem. Eng. J.*, 2022, **433**, 133841.
25 S. Ohno, U. Aydemir, M. Amsler, J. H. Pöhls, S. Chanakian, A. Zevalkink, M. A. White, S. K. Bux, C. Wolverton and G. J. Snyder, *Adv. Funct. Mater.*, 2017, **27**, 1606361.
26 Z. Wu, J. Li, X. Li, M. Zhu, K. C. Wu, X. T. Tao, B. B. Huang and S. Q. Xia, *Chem. Mater.*, 2016, **28**, 6917–6924.
27 S. Bobev, J. D. Thompson, J. L. Sarrao, M. M. Olmstead, H. Hope and S. M. Kauzlarich, *Inorg. Chem.*, 2004, **43**, 5044–5052.
28 C. Chen, W. Xue, X. Li, Y. Lan, Z. Zhang, X. Wang, F. Zhang, H. Yao, S. Li, J. Sui, P. Han, X. Liu, F. Cao, Y. Wang and Q. Zhang, *ACS Appl. Mater. Int.*, 2019, **11**, 37741–37747.
29 J. Zhang, Z. Wu and S. Xia, *Chin. Sci. Bull.*, 2019, **64**, 1679–1690.
30 C. Chen, W. Xue, S. Li, Z. Zhang, X. Li, X. Wang, Y. Liu, J. Sui, X. Liu, F. Cao, Z. Ren, C. W. Chu, Y. Wang and Q. Zhang, *Proc. Natl. Acad. Sci. U. S. A.*, 2019, **116**, 2831–2836.
31 D. Lützenkirchen-Hecht, B. Gržeta, M. Vrankić, S. Bosnar, A. Šarić, D. Petrov and R. Wagner, *Part 1: XANES studies, 12th DELTA User Meeting*, 2016, pp. 91–92.
32 G. Moreau, R. Scopelliti, L. Helm, J. Purans and A. E. Merbach, *J. Phys. Chem. A*, 2002, **106**, 9612–9622.
33 S. Carlson, J. Hölsä, T. Laamanen, M. Lastusaari, M. Malkamäki, J. Niittykoski and R. Valtonen, *Opt. Mater.*, 2009, **31**, 1877–1879.
34 W. Klemm, *Proc. Chem. Soc. Lond.*, 1958, **12**, 329–341.
35 A. He, E. L. K. Wille, L. M. Moreau, S. M. Thomas, J. M. Lawrence, E. D. Bauer, C. H. Booth and S. M. Kauzlarich, *Phys. Rev. Mater.*, 2020, **4**, 114407.
36 K. Li, Z. Li, L. Yang, C. Xiao and Y. Xie, *Inorg. Chem.*, 2019, **58**, 9205–9212.
37 T. Lyu, Q. X. Yang, F. C. Meng, J. He, A. Benton, C. Chronister, Z. Li and G. Y. Xu, *Chem. Eng. J.*, 2021, **404**, 126925.
38 K. Luo, M. R. Roberts, R. Hao, N. Guerrini, D. M. Pickup, Y.-S. Liu, K. Edström, J. Guo, A. V. Chadwick, L. C. Duda and P. G. Bruce, *Nat. Chem.*, 2016, **8**, 684–691.
39 Z. W. Lebens-Higgins, N. V. Faenza, M. D. Radin, H. Liu, S. Sallis, J. Rana, J. Vinckeviciute, P. J. Reeves, M. J. Zuba, F. Badway, N. Pereira, K. W. Chapman, T.-L. Lee, T. Wu, C. P. Grey, B. C. Melot, A. V. D. Ven, G. G. Amatucci, W. Yang and L. F. J. Piper, *Mater. Horiz.*, 2019, **6**, 2112–2123.
40 S. Q. Xia and S. Bobev, *J. Am. Chem. Soc.*, 2007, **129**, 10011–10018.